U-Pb monazite ages of the Kabanga mafic-ultramafic intrusions and contact aureoles, central Africa: geochronological and tectonic implications

Jian-Wei Zi[1,2*], Birger Rasmussen[1,3], Janet R. Muhling[3], Wolfgang D. Maier[4], Ian R. Fletcher[2]

[1] State Key Lab of Geological Processes and Mineral Resources, China University of Geosciences, Wuhan 430074, China

[2] John de Laeter Centre, Curtin University, Kent Street, Bentley, WA 6102, Australia

[3] School of Earth Sciences, The University of Western Australia, Stirling Highway, Perth, WA 6009, Australia

[4] School of Earth and Ocean Sciences, Cardiff University, Park Place, Cardiff CF10 3AT, UK

*corresponding author (zijw@hotmail.com)

ABSTRACT

Mafic-ultramafic rocks of the Kabanga-Musongati (KM) alignment in the East African Nickel Belt occur as Bushveld-type layered intrusions emplaced in metasedimentary sequences. The age of the mafic-ultramafic intrusions remains poorly constrained, though they are regarded to be part of ca. 1375 Ma bimodal magmatism dominated by voluminous S-type granites. In this study, we investigate igneous monazite and zircon from a differentiated layered intrusion and metamorphic monazite from the contact aureole. The monazite shows contrasting crystal morphology, chemical composition and U-Pb age. Monazite formed by contact metamorphism in response to emplacement of mafic-ultramafic melts is characterized by extremely high Th and U, and yielded a weighted mean $^{207}Pb/^{206}Pb$ age of 1402 ± 9 Ma, which is in agreement with dates from the igneous monazite and zircon. The ages indicate that the intrusion of ultramafic melts was substantially earlier (by approximately 25 million years, 95% confidence) than the prevailing S-type granites, calling for a reappraisal of the previously suggested model of coeval, bimodal magmatism. Monazite in the metapelitic rocks also records two younger growth events at ca. 1375 Ma and ca. 990 Ma, coeval with metamorphism during emplacement of S-type granites and tin-bearing granites, respectively. In conjunction with available geologic evidence, we propose that the KM mafic-ultramafic intrusions likely heralded a structurally controlled thermal anomaly related to Nuna breakup, which culminated during the ca. 1375 Ma Kibaran event manifested as extensive intracrustal melting in the adjoining Karagwe-Ankole Belt (KAB), producing voluminous S-type granites. The Grenvillian-aged (ca. 990 Ma) tin-bearing granite and related Sn

mineralization appear to be the far-field record of tectonothermal events associated with collision along the Irumide Belt during Rodinia assembly. Since monazite is a ubiquitous trace phase in pelitic sedimentary rocks in contact aureoles of mafic-ultramafic intrusions or in regional metamorphic belts, our study highlights the potential of using metamorphic monazite to determine ages of mafic-ultramafic intrusions, and to reconstruct post-emplacement metamorphic history of the host terranes.

Key words: U-Pb monazite geochronology; Mafic-ultramafic intrusions; Karagwe-Ankole Belt; Kabanga; Nuna breakup; Rodinia assembly

INTRODUCTION

Mafic-ultramafic intrusions emplaced in continental terranes indicate regional lithospheric extension, and are typically associated with continental rifting and/or mantle plume activity (Ernst and Buchan, 2001). As such, mafic intrusions (e.g., mafic dike swarms) have played a crucial role in tracing plume-generated large igneous provinces and reconstructing ancient supercontinents (Ernst et al., 2013; Evans, 2013). Mafic-ultramafic intrusive bodies may also be repositories of a variety of base and precious metals (e.g., Ni, Cu, PGEs) that are of significant economic importance (Arndt et al., 2003; Begg et al., 2010). However, obtaining accurate and precise ages from mafic-ultramafic rocks has proven to be challenging due to the scarcity within them of U-bearing accessory minerals suitable for successful dating. Where present, baddeleyite and/or zircon can be used in direct dating of mafic intrusive rocks (Hulbert et al., 2005; Heaman, 2009; Chamberlain et al., 2010; Scoates et al., 2017), but the technique often confronts complications due to the presence of xenocrysts, crustal contamination and metamorphic overprint (Black et al., 1991; Heaman and LeCheminant, 1993; Maier et al., 2015). In many cases, it is exceedingly difficult to assemble an adequate number of crystals for analysis because of their extremely low quantities and small crystal size. Another U-bearing zirconium phase, zirconolite, has been shown to be a robust chronometer that can be used to date mafic rocks (Rasmussen and Fletcher, 2004; Rasmussen et al., 2009), yet the usefulness of this technique is limited by the restricted occurrence of the mineral and post-crystallization alteration. Other techniques such as Ar-Ar, Sm-Nd, and Rb-Sr are considered less reliable due to their susceptibility to later thermal resetting, a problem particularly acute for Precambrian rocks that have typically endured extensive alteration.

Intrusion of mafic-ultramafic rocks commonly induces contact metamorphism and/or partial melting of country rocks which may lead to new growth of U-bearing minerals (e.g., zircon and monazite), bestowing a useful 'indirect' approach for determining the timing of emplacement of the intrusions. In a study of Proterozoic mafic-ultramafic intrusions in the Sveconorwegian Province, SW Sweden, Scherstén et al. (2000) derived ages of the intrusions by analyzing newly crystallized zircon grains and overgrowths on xenocrysts in the country rocks. This indirect dating approach has been advanced through investigation of other mineral phases such as monazite. As a versatile chronometer, monazite is well-known for its capability of recording a wide range of geological processes from granitic magmatism and high-grade metamorphism to low-grade hydrothermal infiltration and related mineralization (Parrish, 1990; Williams et al., 2007), because it is susceptible to dissolution-reprecipitation induced by tectonic and thermal events over prolonged periods (Williams, 2001; Rasmussen and Muhling, 2007; Harlov et al., 2011; Williams et al., 2011; Seydoux-Guillaume et al., 2012). By dating metamorphic monazite crystals within a contact aureole, U-Pb ages that correspond to the timing of magma emplacement can be obtained. This approach has proven to be applicable to determining ages of intrusions of various types such as mafic intrusions (Rasmussen and Fletcher, 2002), granite plutons (Rasmussen et al., 2001; Ayers et al., 2013) and an alkaline-carbonatite complex (Zi et al., 2017).

In this paper, we further explore the potential of monazite in revealing the intricate history of igneous intrusions particularly in areas that have experienced multiple magmatic-metamorphic events. The Kabanga-Musongati alignment in Tanzania and Burundi is ideal for such a study because it is characterized by mafic-ultramafic intrusions and granite plutons emplaced into sedimentary rocks. Existing geochronological data in the region indicate a predominant episode of igneous activity at ca. 1375 Ma, interpreted to be a single bimodal magmatism marking the Kibaran event (Tack et al., 2010). However, the age constraints are mainly from granitoids, and there is evidence that the mafic-ultramafic layered intrusions, which host world-class nickel sulfide deposits, must have predated the granites (Evans et al., 1999; Maier et al., 2007; Maier et al., 2010). In this study, we mainly target monazite in the sedimentary rocks that have been affected by contact metamorphism in response to igneous intrusions, and establish a precise record of the history of metamorphic monazite growth, which offers new insights into the timing and geodynamic context of the igneous intrusions and related Ni-PGE mineralization. The geochronology data reported in this contribution, integrated with available geologic evidence, allows recognition of multiple episodes of igneous/metamorphic events which are readily correlated with contemporaneous global-scale magmatism in the context of tectonic transition from Nuna to Rodinia configuration.

GEOLOGICAL BACKGROUND

Geological setting

Largely based on geophysical imagery, basin stratigraphy and provenance analysis (Tack et al., 2010; Fernandez-Alonso et al., 2012), the NE-trending, >1000 km long orogenic belt between the Congo and Tanzania cratons has recently been subdivided into two segments, namely the Karagwe-Ankole Belt (KAB) in the NE and the Kibaran Belt (KIB) in the SW, separated by the NW-trending Paleoproterozoic Ubende-Rusizi belt (Fig. 1). The KAB comprises two structurally contrasting domains: the Western Domain (WD) and the Eastern Domain (ED), bounded by the NE-SW trending Kabanga-Musongati (KM) alignment (Fig. 1).

The KM alignment is characterized by a series of mafic-ultramafic intrusions emplaced in thick metasedimentary rocks. The southwestern continuation of the mafic-ultramafic intrusions is truncated by Lake Tanganyika, a possible western arm of the East African Rift Valley (Evans et al., 2016), whereas the Kapalagulu intrusion, located on the eastern shore of Lake Tanganyika (Fig. 1), is considered a southern extension of the KM intrusions (Maier et al., 2008). The mafic-ultramafic intrusions of the KM alignment host large nickel deposits and form the major components of the East African Nickel Belt (Evans et al., 2016), which is also known as the Central African Nickel Belt (Wilhelmij and Cabri, 2016).

Within the KM alignment and its vicinity, well-differentiated, Bushveld-type layered intrusions are accompanied by small chonoliths, as well as poorly differentiated, gabbronorite dykes and sills (Fig. 1). The layered mafic-ultramafic intrusions are composed of dunite, peridotite, pyroxenite, gabbronorite and anorthosite, showing magmatic layering and cumulate textures, and contact metamorphic aureoles in the host rocks (Deblond and Tack, 1999; Duchesne et al., 2004; Maier et al., 2008). The intrusions are thought to have crystallized from a mantle-derived, high-Mg picritic or basaltic magma, with various amounts of crustal assimilation (Evans et al., 1999; Duchesne et al., 2004; Maier et al., 2008), though Duchesne et al. (2004) also invoked a sub-continental lithospheric mantle source to explain the enriched Nd isotopic signatures ($\varepsilon_{Nd}(t)$ values of -8 to -3) observed in some gabbronorite intrusions. The intrusions contain abundant sulfides, pyrrhotite, pentlandite, and lesser amounts of chalcopyrite and pyrite (Evans et al., 1999; Maier et al., 2010), forming the significant nickel sulfide deposits of the East African Nickel Belt. The Kapalagulu intrusion also contains high-grade platinum-group-element (PGE) mineralization associated with chromitite and sulfide-bearing harzburgite (Maier et al., 2008; Wilhelmij and Cabri, 2016).

The mafic-ultramafic intrusions were emplaced within metasedimentary rocks of the Karagwe-Ankole sedimentary sequences that unconformably rest on the Archean-early Proterozoic basement of the Congo and Tanzania cratons (Maier et al., 2010). The sedimentary sequences are composed of thick successions (up to 5000 m) of alternating arenaceous and pelitic rocks (Maier et al., 2010; Tack et al., 2010).

S-type granites are widespread in areas NW of the KM alignment (Fig. 1). Aeromagnetic anomalies have revealed a series of dolerite dykes emplaced in Archean basement of the NW Tanzania craton and in the Paleoproterozoic Buganda-Toro sequences of SW Uganda, forming the giant, arcuate Lake Victoria dike swarm (Fig. 1). An enriched sub-continental lithospheric mantle source has been proposed for the dike swarm based on geochemical signatures (Mäkitie et al., 2014).

The mafic-ultramafic intrusions appear to have been emplaced prior to the peak stage of the Kibaran event and associated syn-kinematic S-type granitic plutonism (Evans et al., 1999; Evans et al., 2000; Maier et al., 2010), and have been deformed during the latter event. Similar field relationships have been documented by Kokonyangi et al. (2005) in the KIB where mafic intrusions were thermally affected by the emplacement of granites leading to growth of metamorphic mineral assemblage.

Igneous history: existing geochronological constraints

Maier et al. (2007) derived U-Pb zircon ages of 1403 ± 14 Ma for the Kabanga North intrusion, and 1392 ± 26 Ma for the Kapalagulu intrusion. Tack et al. (2010) reported U-Pb zircon geochronology results for an amphibole-norite from Musongati, but the majority of the analyses are normally or reversely discordant, which is ascribed to the combined effects of recent and/or ancient Pb loss and radiation damage caused by high U contents. The most concordant data (within ± 5% discordance) display high dispersion with ages ranging from 1393 ± 12 Ma (1σ) to 1148 ± 50 Ma (1σ), and an older cluster giving a weighted mean ^{207}Pb/^{206}Pb age of 1374 ± 14 Ma (Tack et al., 2010). Hornblende from the same sample records a ^{40}Ar/^{39}Ar age of 1365 ± 2 Ma (Tack et al., 2010). In view of the effect of Pb loss in zircon (as illustrated by the high dispersion) and later thermal overprinting, it is likely that the ^{207}Pb/^{206}Pb zircon age represents a minimum estimate for the age of igneous crystallization of the rock, whereas the ^{40}Ar/^{39}Ar hornblende age may reflect cooling or resetting.

S-type granites from multiple plutons in Burundi and Rwanda yielded zircon ages indistinguishable within analytical uncertainties defining a narrow interval between 1380 Ma and 1370 Ma (Tack et al., 2010). S-type granites and mafic-ultramafic intrusions of similar age have been documented by Kokonyangi et al. (2005) in the KIB (Mitwaba area of the Democratic Republic of Congo), to the SW of the KM alignment. Later igneous activities, including emplacement of A-type granites (Bukirasazi massif, Burundi) at 1207 ± 11 Ma and tin-bearing granites (Kasika massif, DRC) at 986 ± 10 Ma, have been recorded and interpreted as representing minor magmatic additions to the crust (Tack et al., 2010). In the Mitwaba area, Kokonyangi et al. (2004, 2006) have also documented emplacement of tin-bearing granites dated at approximately 1000-950 Ma.

Two dikes of the Lake Victoria dike swarm from SW Uganda provide Sm-Nd isochron ages of 1368 ± 46 Ma and 1374 ± 42 Ma (Mäkitie et al., 2014). The similarity in age led Mäkitie et al. (2014) to suggest that the dike swarm and the ca. 1375 Ma “bimodal” magmatic rocks form a large igneous province related to the break-up of the Nuna supercontinent.

KABANGA LOCAL GEOLOGY AND SAMPLES

Local geology at Kabanga and in the adjoining areas, as well as the morphology and lithological correlation of the Kabanga mafic-ultramafic intrusions, have been described in detail in the literature (Evans et al., 1999; Evans et al., 2000; Maier et al., 2008; Maier et al., 2010; Evans et al., 2016).

A quartzite unit, with a thickness of up to 500 m, occurs as a distinct marker horizon in the footwall of the mafic-ultramafic intrusions at Kabanga (Fig. 2) (Evans et al., 2000; Maier et al., 2010). The quartzite is overlain by andalusite-muscovite-staurolite-biotite schists that locally contain garnet, suggesting a mid-amphibolite facies, high-T/low-P, regional metamorphism (Evans et al., 2000; Maier et al., 2010). Contact metamorphism in the thermal aureoles of the mafic-ultramafic intrusions reached the sillimanite and cordierite-K feldspar facies (Evans et al., 2000) forming narrow, light-colored hornfel zones a few meters in width (Fig. 3A; Maier et al., 2010). Fine-grained, relatively sulfide-poor, banded pelite (Fig. 3C) occurs as discontinuous, 25-75 m thick lenses within the mica schists (Maier et al., 2010).

The intrusions that contain the Kabanga nickel deposit are hosted within steeply-dipping to overturned metasedimentary rocks, and are adjacent to the Bushubi Granite (Fig. 2), which is composed of foliated S-type granite. This granite and its equivalents in the adjacent areas are related to the peak stage of the ca. 1375 Ma Kibaran event (Kokonyangi et al., 2004; Kokonyangi et al., 2005; Buchwaldt et al., 2008; Tack et al., 2010). The sedimentary sequence is made up predominantly of metapelites and metasiltstones (shales and schists), within minor arenitic metasandstones (quartzites). The metapelite rocks are graphitic in places and can contain up to 5 modal % of pyrrhotite as thin layer-parallel laminae and lenses. They are schistose to phyllitic, with the metamorphic fabric dipping steeply to the WNW. The metamorphic grade decreases from amphibolite facies adjacent to the granite, to lower greenschist facies farther away to the east (Evans et al., 2016).

Despite intense weathering and thrusting of the sedimentary sequence at surface, the host rocks immediate to the Kabanga intrusions have been intersected in several deep drill-holes (Fig. 2; Evans et al., 2000; Maier et al., 2010). A total of five metasedimentary samples in the vicinity of the layered intrusions at Kabanga and Nyanzali were selected in this study, including muscovite schist samples K89 (drill-hole NYZD 002, drill-depth 193.1 m), K96 (KN 01-01B, 1356.15 m), K99 (KSM 06, 68.86 m) and K100 (KSM 06, 125.4 m), and a banded pelite sample K101 (KSM 04, 150.4 m). Also included is a pegmatoidal gabbronorite sample WM5 from Kabanga Main (drill-hole KN95-78, drill-depth 211.1 m), which forms a component of the layered intrusions, and comprises up to about 1 cm long pyroxene crystals in a dark matrix of primarily plagioclase and pyroxene.

ANALYTICAL METHOD

In situ U-Pb dating was conducted on monazite and zircon in the selected rock samples from Kabanga using the Sensitive High-Resolution Ion MicroProbe (SHRIMP II) housed at the John de Laeter Centre, Curtin University. Monazite analytical procedures are described and discussed in detail by Fletcher et al. (2010), and outlined in the Supplementary Information. Monazite reference standards (French, Z2908, Z2234, QMa28-1, PD-95) were in a separate mount that was cleaned and Au-coated with the sample mounts for each analytical session. SHRIMP operational settings and calibration parameters are summarized in Table S1. Zircon analytical procedures are similar to those applied by Rasmussen and Fletcher (2010) for *in situ* analysis of small grains. Fragments of the calibration reference zircon CZ3 were set in a 3-mm-diameter polished disc cast into the zircon sample mount.

SHRIMP U-Pb data were reduced with Squid-2 software (Ludwig, 2009) using spot average values for all ratios. A conventional exponential calibration procedure (exp. = 2.0) was used for $^{206}Pb/^{238}U$ in zircon, and 1-D calibrations of $^{206}Pb^+/^{270}[UO_2]^+$ and $^{208}Pb^+/^{264}[ThO_2]^+$ were used for monazite $^{206}Pb/^{238}U$ and $^{208}Pb/^{232}Th$, respectively (Fletcher et al., 2010). Corrections for U, Th, Pb and REE matrix effects in monazite Pb/U and Pb/Th, and renormalization of monazite $^{207}Pb/^{206}Pb$ data, were carried out subsequently applying established protocols (Fletcher et al., 2010). Data plots were prepared using Isoplot-3 (Ludwig, 2012). Individual analyses in concordia plots are displayed with 1σ errors, whereas weighted mean dates are quoted with 95% confidence limits, unless otherwise specified.

RESULTS

Contrasting morphology and compositions of monazite

Monazite in the gabbronorite sample WM5 occurs as euhedral or subhedral crystals, up to 60 μm long, with aspect ratios between 2:1 and 3:1 (Fig. 4A, B). They show uniform Th abundances averaged at 35,000 ppm and Th/U of 45, typical of igneous monazite (e.g., Zi et al., 2018). The monazite exhibits pleochroic haloes in biotite (Fig. 3D). Acicular zircon crystals or crystal aggregates also occur in this sample (Figs. 3D and 4C).

Monazite in muscovite schists from the Kabanga area displays two distinct modes of crystal habit: discrete minute, hypidioblastic to xenoblastic grains (<30 μm, Fig. 5A-C), and large, skeletal aggregates (>300 μm across; Figs. 5D, 6A-C). Consistently, these two types of monazite show marked differences in U and, in particular, Th concentrations (Fig. 7). The minute monazite (e.g., sample K99 in Fig. 5A) is homogeneous in back-scattered electron (BSE) images, with no or minimal inclusions. They have significantly higher Th and U relative to the skeletal monazite (K89 and K96). The compositional contrast is best illustrated by sample K100 in which both types of monazite are observed (Fig. 5C, D), and the difference in Th between the two types is greater than an order of magnitude (Fig. 7).

Multiple generations of monazite growth

U-Pb geochronology results are summarized in this section and in Table 1; full datasets are provided in the Data Repository (Tables DR1-DR7). The results are integrated with previously published geochronology data (compiled in Table S2) for comparison purposes and to establish a complete history for the emplacement of the igneous intrusions and associated metamorphic-hydrothermal activities.

Igneous monazite and zircon

Monazite and zircon were identified in the gabbronorite sample (WM5) (Figs. 3D, 4A-C). Twenty-seven analyses were collected from five monazite grains, among which one analysis shows >1% common ^{206}Pb and >5% discordance and was thus excluded in age calculation. The rest give a weighted mean $^{207}Pb/^{206}Pb$ date of 1391 ± 9 Ma (*n* = 26, MSWD = 1.5) and weighted mean $^{206}Pb/^{238}U$ date of 1395 ± 10 Ma (MSWD = 2.0) (Fig. 4D), with the former being considered a better approximation of the timing of monazite growth.

A total of 22 spot analyses were obtained on zircon from this sample; five of them record >5% discordance and/or >1% common ^{206}Pb and hence are disregarded in age determinations. The remaining 17 analyses, from nine zircon grains, have a weighted mean $^{207}Pb/^{206}Pb$ date of 1387 ± 10 Ma (MSWD = 0.85) and mean $^{206}Pb/^{238}U$ date of 1395 ± 18 Ma (MSWD = 0.83). It is noted that most of the data show slight reverse discordance (Fig. 4E), likely reflecting some extent of mass fractionation related to matrix effect. The mean $^{207}Pb/^{206}Pb$ date of 1387 ± 10 Ma is taken as the zircon crystallization age.

Monazite and zircon in this sample show unequivocal characteristics of igneous origin, and both are consistently uniform in Th and U chemistry, indicating a single generation of each mineral. As the mean $^{207}Pb/^{206}Pb$ dates of zircon and monazite are mutually indistinguishable within analytical uncertainties, the datasets from the two independent chronometers can be pooled to give a weighted mean $^{207}Pb/^{206}Pb$ date of 1389.5 ± 6.2 Ma (*n* = 43, MSWD = 1.2), rounding to 1390 ± 7 Ma, which is considered as the best estimate of the age of igneous crystallization.

Metamorphic monazite

Monazite crystals in polished thin sections made from five metapelite (muscovite schist and banded pelite) samples were analyzed. They occur as authigenic grains surrounded by, and intergrown with, other metamorphic minerals. As shown in Figures 5-8, the abundance, grain size, crystal morphology and texture, chemical composition, and U-Th-Pb ages of the authigenic monazite all vary as a function of metamorphic grade and host lithology, and allow classification into three types corresponding to three episodes of monazite growth, referred to as M-I, M-II, and M-III (Table 1).

M-I monazite, K99 and K100

M-I monazite occurs as discrete, minute (10–30 μm), hypidioblastic to xenoblastic crystals in muscovite schist samples K99 and K100 (Fig. 5A, C) collected from the upper portion of the Kabanga Main intrusion, and is characterized by markedly high Th and U (typically >100,000 ppm and >2,000 ppm, respectively), with high Th/U values (most >50) (Fig. 7). Eight analyses on 7 grains from the two samples display a significant variation in radiogenic ^{238}U/^{206}Pb, but their radiogenic ^{207}Pb/^{206}Pb define a restricted range (Fig. 5E), suggesting that all the grains are of the same age, but have lost variable amounts of radiogenic Pb. Thorium-rich monazite has been shown to be more susceptible to alteration than its Th-poor counterpart, likely due to greater chemical disequilibrium at low temperatures or to radiation-induced partial metamictization given the exceedingly high Th contents (Berger et al., 2008). Excluding distinct outliers in ^{207}Pb/^{206}Pb, 8 analyses define an array subparallel to the ^{238}U/^{206}Pb axis, only two of the ^{238}U/^{206}Pb apparent ages are within 10% discordance, suggesting that almost all of the analyzed areas are

Pb deficient. The overall spread of the high-Th analyses in the concordia diagram (Fig. 5E) suggests that Pb loss has resulted from a combination of both geologically ancient and recent events. In that case, the best estimate of the crystallisation age is given by the weighted mean $^{207}Pb/^{206}Pb$ date, 1402 ± 9 Ma (n = 8, MSWD = 0.33).

Monazite grain 0911K from sample K99 shows crystal morphology (elongate, Fig. 5B) and Th-U chemistry (relatively low Th/U = 9, Fig. 7) distinct from other grains, and one analysis on this grain yielded a $^{207}Pb/^{206}Pb$ date of 1378 ± 5 Ma (1σ), significantly younger than other grains from the same sample but similar to the M-II monazite (see below). Monazite grain 0911A from sample K100 displays an inclusion-bearing core enclosed by a brighter, inclusion-free rim that shows a hypidioblastic crystal outline (Fig. 5C). The rim is characterized by elevated Th and U (but lower Th/U ratio) compared with the core, and possibly formed through dissolution-reprecipitation during a younger metamorphic/hydrothermal event. Consistently, the spot analysis (0911A.1-1) on the rim yielded a $^{207}Pb/^{206}Pb$ date of 1379 ± 8 Ma (1σ) which is comparable with that recorded by grain 0911K.

M-II monazite, K100, K89 and K96

M-II monazite occurs as large (>300 μm), round or lozenge-shaped poikiloblasts displaying skeletal textures (Figs. 5D, 6A-C), and mainly occurs in samples K89 and K96, but is also seen in K100. These monazite grains are characterized by lower Th and U contents (<10,000 ppm and <1,000 ppm, respectively) with Th/U ratios typically <30 (Fig. 7). The marked similarities in crystal texture and Th-U chemistry indicate that these grains likely formed from the same metamorphic event.

Six analyses were taken from a skeletal grain in K100. Excluding 2 analyses which record >1% common ^{206}Pb or >10% reverse discordance and one outlier, the rest yielded ^{207}Pb/^{206}Pb dates ranging from 1376 Ma to 1302 Ma; these together with the single analysis from the rim of monazite grain 0911A (Fig. 5C) in this sample, result in a weighted mean ^{207}Pb/^{206}Pb date of 1375 ± 15 Ma (*n* = 4, MSWD = 1.08) (Fig. 5E).

Twenty analyses were taken from three aggregate grains in sample K89. Uranium and Th contents in these grains are low and variable, leading to poor precision in age determination. Only 5 analyses have <1% common ^{206}Pb and are within 5% of apparent discordance. They give a weighted mean ^{207}Pb/^{206}Pb date of 1369 ± 34 Ma (MSWD = 1.09), but their ^{206}Pb/^{238}U ratios are scattered (Fig. 6D). Applying less rigorous criteria, if the 4 analyses that show slightly >1% common ^{206}Pb or marginally >5% discordance are taken into account, the weighted mean ^{207}Pb/^{206}Pb age becomes 1379 ± 27 Ma (*n* = 9, MSWD = 1.1).

Twenty analyses performed on monazite in muscovite schist sample K96 show overall uniformity of both U-Th compositions and U-Pb ages, indicating a single generation. However, 6 analyses failed to satisfy the data screen criteria with regard to common Pb and discordance levels, and thus were disregarded in age determinations. The remaining 14 analyses yielded a weighted mean ^{207}Pb/^{206}Pb date of 1374 ± 13 Ma (MSWD = 0.73) (Fig. 6E).

Pooled together, M-II monazite from the three samples yielded a weighted mean $^{207}Pb/^{206}Pb$ date of 1375 ± 8 Ma (n = 25, MSWD = 1.17), taken as the best estimate of the age of the monazite growth.

M-III monazite, K101

Fourteen analyses were taken from 5 monazite grains in the banded pelite sample K101. Monazite occurs as inclusion-free, xenoblastic crystals in association with biotite and is encased in plagioclase (Fig. 8A-B). The U and Th contents are substantial (Fig. 7), leading to reasonably good precision in $^{207}Pb/^{206}Pb$ despite young ages. All data show appreciable levels of common ^{206}Pb, but none are >1%. Ten analyses are within 5% of discordance, and give a weighted mean $^{207}Pb/^{206}Pb$ date of 991 ± 16 Ma (MSWD = 0.84) (Fig. 7C). Consistently, the weighted mean of the corresponding $^{206}Pb/^{238}U$ dates is 991 ± 11 Ma (n = 10, MSWD = 1.3), and the independently-calibrated weighted mean $^{208}Pb/^{232}Th$ date for the same analyses is 988 ± 31 Ma. The mean $^{207}Pb/^{206}Pb$ date of 991 ± 16 Ma is the preferred age of the M-III monazite.

DISCUSSION

Links between monazite growth and intrusion events

Characterization based on crystal morphology and textural relationships indicates that all the sedimentary rock-hosted monazite investigated in this study is metamorphic in origin. The monazite is contained in samples that comprise minerals clearly of metamorphic origin, including recrystallized feldspar and sulfide minerals. Triple junctions and/or interfingering textures observed between metamorphic monazite and surrounding minerals (Figs. 5, 6, 8) indicate simultaneous growth.

The amount of Th in monazite from different rocks is widely variable, and a correlation between Th abundance and metamorphic grade has long been recognized (Overstreet, 1967), indicating that the variation of Th in monazite is controlled by temperature-pressure conditions during metamorphism. Numerous studies have shown that monazite precipitated in low-grade metamorphic or hydrothermal environments typically has less than 1 wt.% ThO_2, whereas that from high-grade (amphibolite facies or higher) rocks can contain up to 9 wt.% ThO_2 (Overstreet, 1967; Rasmussen et al., 2001; Rasmussen and Fletcher, 2002; Schandl and Gorton, 2004; Zi et al., 2015). The elevation of Th contents in high-grade monazite (Overstreet, 1967) likely reflects the release of Th (and U) into metamorphic fluids by mineral reactions (e.g., dissolution of detrital monazite), which also supplied the REEs and phosphorous for the growth of authigenic monazite (Rasmussen and Muhling, 2007; Rasmussen and Muhling, 2009).

The high- and low-Th monazite identified in the metasedimentary host rocks of the igneous intrusions at Kabanga yielded two distinct U-Pb ages, 1402 ± 9 Ma and 1375 ± 8 Ma, respectively (Figs. 8 & 9). It is straightforward that the minute, inclusion-free, monazite crystals (M-I) characterized by Th enrichment were formed in high-grade contact metamorphic aureoles around the mafic-ultramafic intrusions at ca. 1400 Ma, a date convergent with results from the igneous monazite and zircon (Figs. 9 & 10). The monazite grains (M-II) that display Th-depletion and skeletal textures most likely crystallized as a consequence of low-grade metamorphism, as also supported by the xenoblastic and inclusion-rich habit of these crystals. The low-grade metamorphic activity at ca. 1375 Ma is more regional in nature and is temporally and spatially related to emplacement of the S-type granites in the KAB.

The M-III monazite, dated at 991 ± 16 Ma, from sample K101 shows moderate Th and U compositions (Fig. 7) and its growth is readily linked to a metamorphic/hydrothermal episode synchronous with the emplacement of the tin-bearing granites and related regional-scale Sn mineralization in both the KAB and KIB (Pohl, 1994; Kokonyangi et al., 2004; Kokonyangi et al., 2006; Tack et al., 2010). Similar ages are also recorded by metamorphic zircon rims (966 ± 11 Ma), from a S-type granite in the Kilimbi-Muzimu massif of the KAB (Tack et al., 2010), suggesting regional-scale metamorphism, which gave rise to the ca. 990 Ma monazite in the banded pelite at Kabanga.

An updated igneous history: bimodal, but not coeval

Earlier geochronology work carried out by Tack et al. (1994) yielded an emplacement age of ca. 1275 Ma (U-Pb zircon age of an amphibole norite from Musongati) for the KM mafic-ultramafic rocks, which has been superseded by a new age of 1374 ± 14 Ma obtained from the same sample (Tack et al., 2010). The widespread S-type granites that were imprecisely dated at 1370-1110 Ma have also been narrowed down to 1380-1370 Ma (Fig. 10) (Deblond et al. 2001; Tack et al. 2010 and references therein). Although the large variations in age constraints have caused conflicting interpretations with regard to the mafic-ultramafic intrusions in relation to the S-type granites and regional tectonics (e.g., Pohl, 1994; Tack et al., 1994), the new results of

Tack et al. (2010) led them to propose a short-lived, ca. 1375 Ma Kibaran event that is marked by coeval, bimodal magmatism producing both the mafic-ultramafic intrusions and the S-type granites in the KAB. The generation of the voluminous S-type granites was attributed to concomitant, large-scale crustal melting induced by emplacement of mantle-derived magma (Tack et al., 2010).

Our U-Pb geochronology results from monazite and zircon, however, corroborate zircon ages of ca. 1400 Ma from mafic-ultramafic intrusions at Kabanga North and Kapalagulu (Maier et al., 2007), and suggest that the formation of the mafic-ultramafic intrusions took place approximately 25 million years before the emplacement of voluminous granites at ca. 1375 Ma (Figs. 9 & 10). In support of this interpretation, the youngest detrital zircon from the Muyinga Quartzite in the Western Domain yielded concordant $^{207}Pb/^{206}Pb$ ages of 1421 ± 37 Ma and 1412 ± 21 Ma (1σ), and has been interpreted to represent recycling of an underlying volcanic unit (Fernandez-Alonso et al., 2012). It is likely that this ca. 1.4 Ga volcanism represents the surface expression of KM mafic-ultramafic plutonism. A similar $^{207}Pb/^{206}Pb$ date (1417 ± 2 Ma) has been recorded by zircon from a mafic (orthoamphibolite) complex at Mitwaba in the KIB (Kokonyangi et al., 2005).

The large spread (1393 ± 12 Ma to 1148 ± 50 Ma) shown by the most concordant zircon analyses from an amphibole-norite sample (Mutanga) (Tack et al., 2010) suggest Pb-loss and/or partial resetting of the U-Pb systems during later thermal events, therefore, even the weighted mean age of 1374 ± 14 Ma derived from the oldest cluster likely represents a minimum crystallization age of the rock. This is in agreement with $^{40}Ar/^{39}Ar$ data of 1379-1340 Ma obtained from the mafic-ultramafic intrusions, interpreted as cooling ages of the igneous bodies (Deblond et al., 2001; Tack et al., 2010). The about 25 million-year difference between the weighted mean ages of the mafic-ultramafic intrusions and the S-type granites indicates a significant age gap (Figs. 9 & 10), which is at odds with the proposed “coeval” and “bimodal” nature of the magmatism (Tack et al., 2010). The postulated cogenetic emplacement and geodynamic setting of the mafic and felsic rocks thus also requires re-evaluation.

Tectonic imprints: from Nuna breakup to Rodinia assembly

The ability to determine the intrusive ages of mafic-ultramafic rocks is critically important for supercontinent reconstructions and for the global correlation of ancient mafic magmatic activity worldwide (Ernst et al., 2008; Ernst et al., 2013). On a global scale, the 1.40-1.37 Ga magmatic rocks in the KAB may be compared directly with the contemporaneous components in the different blocks including the Congo Craton (Mayer et al., 2004), Western African Craton (El Bahat et al., 2013), Kalahari (Hanson et al., 2006), Yilgarn (Stark et al., 2018), Siberia, Baltica, and Laurentia (Ernst and Buchan, 2001; Upton et al., 2005; Verbaas et al., 2018), and are correlated to represent mafic magmatic outbursts during the breakup of the Nuna supercontinent (Ernst et al., 2008; Evans and Mitchell, 2011; Pisarevsky et al., 2014).

Mafic-ultramafic layered intrusions at Kabanga, Musongati and Kapalagulu show broad similarities in crystallization sequences and mineral compositions (Maier et al., 2008) and hence have been regarded as an integrated igneous belt approximately 500 km long (Maier et al., 2010). Mafic intrusions typically act as markers of pre-existing crustal weakness and their occurrences as indicators of intraplate crustal extension associated with processes such as subduction (back-arc extension), mantle plume impingement and continental rifting during supercontinent breakup (e.g., Wilson, 1992; Ernst et al., 2013). Geochemical characteristics of the KM intrusions indicate a parental magma predominantly derived from the asthenospheric mantle with appreciable assimilation of pelitic sedimentary rocks during magma ascent and emplacement, leading to sulfide enrichment of the intrusions (Maier et al., 2010). Mäkitie et al. (2014) correlate these mafic-ultramafic intrusions to the arcuate mafic dikes (the Lake Victoria dike swarm) in the periphery of the KAB (Fig. 1) and suggest that they collectively form a large igneous province, despite the considerable differences in geochemistry of the two suites. However, synchroneity between the dike swarm and the ca. 1.4 Ga mafic-ultramafic intrusions remains to be confirmed, considering the large uncertainties of the available Sm-Nd isochron age constraints for the dike swarm (1368 ± 41 Ma and 1374 ± 42 Ma; Mäkitie et al., 2014).

The ‘Wilson-style orogenic’ or ‘active margin’ model previously proposed for the Mesoproterozoic evolution of the KAB was refuted by Fernandez-Alonso et al. (2012) who, largely based on regional correlation of basin stratigraphy and depositional history, argue for an intracratonic setting for the KAB since the Paleoproterozoic (ca. 1.8 Ga) formation of a united ‘proto-Congo Craton’. Instead, the linear distribution of the mafic-ultramafic intrusions along the western margin of the Tanzania Craton is consistent with a lithospheric-scale structural control, in an extensional regime, to allow emplacement of the mantle-derived melts into the KAB pelitic sedimentary rocks. Stratigraphic successions and provenance analysis of the KAB suggest that the attempted rifting was aborted (Fernandez-Alonso et al., 2012), and that the mafic-ultramafic intrusions and the subsequent intracrustal melting, exemplified by the S-type granitic plutonism during peak Kibaran event at ca. 1375 Ma (Tack et al., 2010), likely marked the final consolidation of this part of the assembled proto-Congo Craton (Fernandez-Alonso et al., 2012).

Renewed crustal melting took place at ca. 990 Ma, possibly after an episode of A-type granite plutonism at ca. 1205 Ma (Tack et al., 2010), and gave rise to regional-scale tin-bearing granites and numerous pegmatitic and quartz veins rich in Sn, W, and rare metals (Cahen et al., 1984; Pohl, 1994). The tin-bearing granites and associated mineralization are related to a compressive deformation (the S2-fabric as documented by Fernandez-Alonso et al. (2012); see also Pohl (1994)) which is considered a far-field effect from the Irumide Belt during amalgamation of the Rodinia supercontinent (De Waele et al., 2003; Johnson et al., 2005), although whether or not the proto-Congo Craton (including the KAB) was a component of Rodinia, remains an open question (De Waele et al., 2008; Pisarevsky et al., 2014).

Implications for dating mafic-ultramafic intrusions by monazite

The interaction between hot intrusions and surrounding sediments leads to contact metamorphism (Einsele et al., 1980) that results in the growth of authigenic monazite (Williams, 2001; Rasmussen and Fletcher, 2002). Our study demonstrates that metamorphic monazite in hornfels (contact aureoles) can be dated *in situ* by ion microprobe using a small ablation spot. By characterizing textural relationships, crystal morphology and chemistry, multiple generations of monazite can be distinguished and linked to regional-scale tectonic and magmatic activities that provided the heat and fluids for their growth. Therefore, U-Pb dating of metamorphic monazite in hornfels are capable of not only constraining individual intrusion events, but also providing a more complete picture of the metamorphic history of the host terrane.

Ni (-PGE) mineralization is genetically related to igneous processes of mafic-ultramafic intrusions (Naldrett, 1999, 2010). The mafic-ultramafic bodies hosting the nickel sulfide and PGE deposits are typically small and irregular in dimension, and precise geochronology is essential to understanding the emplacement history and geodynamic setting of the intrusions, which help to locate mineralized intrusive bodies (Maier and Groves, 2011). The results of this study demonstrate the potential of using monazite from hornfels adjoining mineralized mafic-ultramafic rocks to precisely constrain the timing and duration of mafic-ultramafic magmatism in the East African Nickel Belt and assess the relationships between mafic-ultramafic and granitic magmatism. The approach employed in the present study, therefore, provides an additional avenue for resolving the commonly complicated magmatic and metamorphic history of economically important intrusions as well as the regional tectonothermal history of the host terranes.

CONCLUSIONS

Precise and accurate dating of mafic-ultramafic intrusive rocks has been one of the most challenging and controversial aspects in attempting to understand their geology and nickel sulfide mineralization. Using the KM alignment of the East African Nickel Belt as an example, we report the U-Pb geochronology of metamorphic monazite in contact aureoles of mineralized mafic-ultramafic intrusions. *In situ* U-Pb geochronology of monazite crystals reveals three episodes of metamorphism in the KAB, including: i) Contact metamorphism (ca. 1400 Ma) related to the mafic-ultramafic intrusions; ii) a regional metamorphic event (ca. 1375 Ma) linked to intracrustal melting and intrusion of S-type granites; iii) a regional metamorphic event (ca. 990 Ma) that was accompanied by intracrustal melting to produce the tin-bearing granites.

In particular, the documentation of metamorphic monazite in hornfels of the mafic-ultramafic intrusions is significant as a means of establishing indirect emplacement ages, to circumvent difficulties of directly dating such rocks. The similarity of the metamorphic monazite ages and those from igneous monazite and zircon in a differentiated phase of the intrusions adds confidence to the reliability of the technique. Despite the overlap in ranges between some of the age determinations, the mean ages acquired in this study, i.e., the ca. 1400 Ma for contact metamorphism associated with the mafic-ultramafic rocks and ca. 1375 Ma syn-Kibaran metamorphism, are consistent with the crosscutting relationships between the KM mafic-ultramafic intrusions and the S-type granites, indicating a substantial age difference of approximately 25 million years. As such, monazite in metamorphosed sedimentary rocks not only provide age records that perfectly match known igneous history, but also resolve that the mafic-ultramafic layered intrusions significantly predated the pervasive granitic magmatism, thus invalidating the coeval bimodal model (the ca. 1375 Ma Kibaran event) as previously proposed.

The ca. 1400 Ma mafic-ultramafic intrusions and the following granitic plutonism during the ca. 1375 Ma Kibaran event in the KAB and adjoining areas represent a significant component of the global-scale igneous event which is linked to the breakup of the Nuna supercontinent. The renewed crustal melting that gave rise to the ca. 990 Ma tin-bearing granites is readily ascribed to tectonic imprint related to collision processes along the Irumide Belt during Rodinia assembly.

ACKNOWLEDGMENTS

JWZ and BR were funded by the MOST Special Funds through the State Key Lab of Geological Processes and Mineral Resources (MSFGPMR19, GPMR201802) and by the National Natural Science Foundation of China (41873062). We acknowledge the facilities, and technical assistance of the John de Laeter Centre, and the Centre for Microscopy, Characterisation & Analysis at the University of Western Australia. We are grateful to Nicole Rayner, an anonymous reviewer and the Associate Editor for their constructive comments and suggestions which greatly enhanced the paper.

REFERENCES CITED

Arndt, N. T., Czamanske, G. K., Walker, R. J., Chauvel, C., and Fedorenko, V. A., 2003, Geochemistry and Origin of the Intrusive Hosts of the Noril'sk-Talnakh Cu-Ni-PGE Sulfide Deposits: Economic Geology, v. 98, no. 3, p. 495-515.

Ayers, J. C., Crombie, S., Loflin, M., Miller, C. F., and Luo, Y., 2013, Country rock monazite response to intrusion of the Searchlight pluton, southern Nevada: American Journal of Science, v. 313, no. 4, p. 345-394.

Begg, G. C., Hronsky, J. A. M., Arndt, N. T., Griffin, W. L., O'Reilly, S. Y., and Hayward, N., 2010, Lithospheric, Cratonic, and Geodynamic Setting of Ni-Cu-PGE Sulfide Deposits: Economic Geology, v. 105, no. 6, p. 1057−1070.

Berger, A., Gnos, E., Janots, E., Fernandez, A., and Giese, J., 2008, Formation and composition of rhabdophane, bastnäsite and hydrated thorium minerals during alteration: Implications for geochronology and low-temperature processes: Chemical Geology, v. 254, no. 3, p. 238-248.

Black, L. P., Kinny, P. D., and Sheraton, J. W., 1991, The difficulties of dating mafic dykes: an Antarctic example: Contributions to Mineralogy and Petrology, v. 109, no. 2, p. 183-194.

Buchwaldt, R., Toulkeridis, T., Todt, W., and Ucakuwun, E. K., 2008, Crustal age domains in the Kibaran belt of SW-Uganda: Combined zircon geochronology and Sm–Nd isotopic investigation: Journal of African Earth Sciences, v. 51, no. 1, p. 4-20.

Cahen, L., Snelling, N. J., Delhal, J., Vail, J. R., Bonhomme, M., and Ledent, D., 1984, The geochronology and evolution of Africa, Oxford, Oxford University Press, 512 p.:

Chamberlain, K. R., Schmitt, A. K., Swapp, S. M., Harrison, T. M., Swoboda-Colberg, N., Bleeker, W., Peterson, T. D., Jefferson, C. W., and Khudoley, A. K., 2010, In situ U–Pb SIMS (IN-SIMS) micro-baddeleyite dating of mafic rocks: Method with examples: Precambrian Research, v. 183, no. 3, p. 379-387.

De Waele, B., Johnson, S. P., and Pisarevsky, S. A., 2008, Palaeoproterozoic to Neoproterozoic growth and evolution of the eastern Congo Craton: Its role in the Rodinia puzzle: Precambrian Research, v. 160, no. 1, p. 127-141.

Deblond, A., Punzalan, L. E., Boven, A., and Tack, L., 2001, The Malagarazi supergroup of southeast Burundi and its correlative Bukoba supergroup of northwest Tanzania: neo- and mesoproterozoic chronostratigraphic constraints from Ar-Ar ages on mafic intrusive rocks: Journal of African Earth Sciences, v. 32, no. 3, p. 435-449.

Deblond, A., and Tack, L., 1999, Main characteristics and review of mineral resources of the Kabanga-Musongati mafic-ultramafic alignment in Burundi: Journal of African Earth Sciences, v. 29, no. 2, p. 313-328.

Duchesne, J.-C., Liégeois, J.-P., Deblond, A., and Tack, L., 2004, Petrogenesis of the Kabanga–Musongati layered mafic–ultramafic intrusions in Burundi (Kibaran Belt): geochemical, Sr–Nd isotopic constraints and Cr–Ni behaviour: Journal of African Earth Sciences, v. 39, no. 3–5, p. 133-145.

Einsele, G., Gieskes, J. M., Curray, J., Moore, D. M., Aguayo, E., Aubry, M.-P., Fornari, D., Guerrero, J., Kastner, M., Kelts, K., Lyle, M., Matoba, Y., Molina-Cruz, A., Niemitz, J., Rueda, J., Saunders, A., Schrader, H., Simoneit, B., and Vacquier, V., 1980, Intrusion of basaltic sills into highly porous sediments, and resulting hydrothermal activity: Nature, v. 283, no. 5746, p. 441-445.

El Bahat, A., Ikenne, M., Söderlund, U., Cousens, B., Youbi, N., Ernst, R., Soulaimani, A., El Janati, M. h., and Hafid, A., 2013, U–Pb baddeleyite ages and geochemistry of dolerite dykes in the Bas Drâa Inlier of the Anti-Atlas of Morocco: Newly identified 1380Ma event in the West African Craton: Lithos, v. 174, p. 85-98.

Ernst, R. E., Bleeker, W., Söderlund, U., and Kerr, A. C., 2013, Large Igneous Provinces and supercontinents: Toward completing the plate tectonic revolution: Lithos, v. 174, no. Supplement C, p. 1-14.

Ernst, R. E., and Buchan, K. L., 2001, Large mafic magmatic events through time and links to mantle-plume heads, *in* Ernst, R. E., and Buchan, K. L., eds., Mantle Plumes: Their Identification Through Time, Volume 352: Boulder, Colorado, p. 483-575.

Ernst, R. E., Wingate, M. T. D., Buchan, K. L., and Li, Z. X., 2008, Global record of 1600–700 Ma Large Igneous Provinces (LIPs): Implications for the reconstruction of the proposed Nuna (Columbia) and Rodinia supercontinents: Precambrian Research, v. 160, no. 1–2, p. 159-178.

Evans, D. A. D., 2013, Reconstructing pre-Pangean supercontinents: Geological Society of America Bulletin, v. 125, no. 11-12, p. 1735-1751.

Evans, D. A. D., and Mitchell, R. N., 2011, Assembly and breakup of the core of Paleoproterozoic–Mesoproterozoic supercontinent Nuna: Geology, v. 39, no. 5, p. 443-446.

Evans, D. M., Boadi, I., Byemelwa, L., Gilligan, J., kabete, J., and Marcet, P., 2000, Kabanga magmatic nickel sulphide deposits, Tanzania: morphology and geochemistry of associated intrusions: Journal of African Earth Sciences, v. 30, no. 3, p. 651-674.

Evans, D. M., Byemelwa, L., and Gilligan, J., 1999, Variability of magmatic sulphide compositions at the Kabanga nickel prospect, Tanzania: Journal of African Earth Sciences, v. 29, no. 2, p. 329-351.

Evans, D. M., Hunt, J. P. P. M., and Simmonds, J. R., 2016, An Overview of Nickel Mineralisation in Africa with Emphasis on the Mesoproterozoic East African Nickel Belt (EANB): Episodes, v. 39, no. 2, p. 319.

Fernandez-Alonso, M., Cutten, H., De Waele, B., Tack, L., Tahon, A., Baudet, D., and Barritt, S. D., 2012, The Mesoproterozoic Karagwe-Ankole Belt (formerly the NE Kibara Belt): The result of prolonged extensional intracratonic basin development punctuated by two short-lived far-field compressional events: Precambrian Research, v. 216, p. 63-86.

Fletcher, I. R., McNaughton, N. J., Davis, W. J., and Rasmussen, B., 2010, Matrix effects and calibration limitations in ion probe U–Pb and Th–Pb dating of monazite: Chemical Geology, v. 270, no. 1–4, p. 31-44.

Hanson, R. E., Harmer, R. E., Blenkinsop, T. G., Bullen, D. S., Dalziel, I. W. D., Gose, W. A., Hall, R. P., Kampunzu, A. B., Key, R. M., Mukwakwami, J., Munyanyiwa, H., Pancake, J. A., Seidel, E. K., and Ward, S. E., 2006, Mesoproterozoic intraplate magmatism in the Kalahari Craton: A review: Journal of African Earth Sciences, v. 46, no. 1, p. 141-167.

Harlov, D., Wirth, R., and Hetherington, C., 2011, Fluid-mediated partial alteration in monazite: the role of coupled dissolution–reprecipitation in element redistribution and mass transfer: Contributions to Mineralogy and Petrology, v. 162, no. 2, p. 329-348.

Heaman, L. M., 2009, The application of U–Pb geochronology to mafic, ultramafic and alkaline rocks: An evaluation of three mineral standards: Chemical Geology, v. 261, no. 1–2, p. 43-52.

Heaman, L. M., and LeCheminant, A. N., 1993, Paragenesis and U-Pb systematics of baddeleyite (ZrO2): Chemical Geology, v. 110, no. 1–3, p. 95-126.

Hulbert, L. J., Hamilton, M. A., Horan, M. F., and Scoates, R. F. J., 2005, U-Pb Zircon and Re-Os Isotope Geochronology of Mineralized Ultramafic Intrusions and Associated Nickel Ores from the Thompson Nickel Belt, Manitoba, Canada: Economic Geology, v. 100, no. 1, p. 29.

Kokonyangi, J., Armstrong, R., Kampunzu, A. B., Yoshida, M., and Okudaira, T., 2004, U–Pb zircon geochronology and petrology of granitoids from Mitwaba (Katanga, Congo): implications for the evolution of the Mesoproterozoic Kibaran belt: Precambrian Research, v. 132, no. 1, p. 79-106.

Kokonyangi, J., Kampunzu, A. B., Poujol, M., Okudaira, T., Yoshida, M., and Shabeer, K. P., 2005, Petrology and geochronology of Mesoproterozoic mafic–intermediate plutonic rocks from Mitwaba (D. R. Congo): implications for the evolution of the Kibaran belt in central Africa: Geological Magazine, v. 142, no. 1, p. 109.

Kokonyangi, J. W., Kampunzu, A. B., Armstrong, R., Yoshida, M., Okudaira, T., Arima, M., and Ngulube, D. A., 2006, The Mesoproterozoic Kibaride belt (Katanga, SE D.R. Congo): Journal of African Earth Sciences, v. 46, no. 1, p. 1-35.

Ludwig, K. R., 2009, Squid 2.50, A User's Manual, Berkeley, Berkeley Geochronology Centre, Berkeley Geochronology Centre Special Publication, 104 p.:

-, 2012, User's Manual for Isoplot 3.75: A geochronological toolkit for Microsoft Excel, Berkeley, Berkeley Geochronology Centre, Berkeley Geochronology Centre Special Publication 75 p.:

Mäkitie, H., Data, G., Isabirye, E., Mänttäri, I., Huhma, H., Klausen, M. B., Pakkanen, L., and Virransalo, P., 2014, Petrology, geochronology and emplacement model of the giant 1.37Ga arcuate Lake Victoria Dyke Swarm on the margin of a large igneous province in eastern Africa: Journal of African Earth Sciences, v. 97, p. 273-296.

Maier, W. D., Barnes, S.-J., Sarkar, A., Ripley, E., Li, C., and Livesey, T., 2010, The Kabanga Ni sulfide deposit, Tanzania: I. Geology, petrography, silicate rock geochemistry, and sulfur and oxygen isotopes: Mineralium Deposita, v. 45, no. 5, p. 419-441.

Maier, W. D., Barnes, S. J., Bandyayera, D., Livesey, T., Li, C., and Ripley, E., 2008, Early Kibaran rift-related mafic–ultramafic magmatism in western Tanzania and Burundi: Petrogenesis and ore potential of the Kapalagulu and Musongati layered intrusions: Lithos, v. 101, no. 1, p. 24-53.

Maier, W. D., and Groves, D. I., 2011, Temporal and spatial controls on the formation of magmatic PGE and Ni–Cu deposits: Mineralium Deposita, v. 46, no. 8, p. 841-857.

Maier, W. D., Peltonen, P., and Livesey, T., 2007, The ages of the Kabanga north and Kapalagulu intrusions, Western Tanzania: a reconnaissance study: Economic Geology, v. 102, no. 1, p. 147.

Maier, W. D., Rasmussen, B., Fletcher, I. R., Godel, B., Barnes, S. J., Fisher, L. A., Yang, S. H., Huhma, H., and Lahaye, Y., 2015, Petrogenesis of the ∼2·77 Ga Monts de Cristal Complex, Gabon: Evidence for Direct Precipitation of Pt-arsenides from Basaltic Magma: Journal of Petrology, v. 56, no. 7, p. 1285-1308.

Mayer, A., Hofmann, A. W., Sinigoi, S., and Morais, E., 2004, Mesoproterozoic Sm-Nd and U-Pb ages for the Kunene Anorthosite Complex of SW Angola: Precambrian Research, v. 133, no. 3-4, p. 187-206.

Naldrett, A. J., 1999, World-class Ni-Cu-PGE deposits: key factors in their genesis: Mineralium Deposita, v. 34, no. 3, p. 227-240.

-, 2010, Secular Variation of Magmatic Sulfide Deposits and Their Source Magmas: Economic Geology, v. 105, no. 3, p. 669.

Overstreet, W. C., 1967, The geologic occurrence of monazite, 530.

Parrish, R. R., 1990, U–Pb dating of monazite and its application to geological problems: Canadian Journal of Earth Sciences, v. 27, no. 11, p. 1431-1450.

Pisarevsky, S. A., Elming, S.-Å., Pesonen, L. J., and Li, Z.-X., 2014, Mesoproterozoic paleogeography: Supercontinent and beyond: Precambrian Research, v. 244, p. 207-225.

Pohl, W., 1994, Metallogeny of the northeastern Kibara belt, Central Africa—Recent perspectives: Ore Geology Reviews, v. 9, no. 2, p. 105-130.

Rasmussen, B., and Fletcher, I. R., 2002, Indirect dating of mafic intrusions by SHRIMP U–Pb analysis of monazite in contact metamorphosed shale: an example from the Palaeoproterozoic Capricorn Orogen, Western Australia: Earth and Planetary Science Letters, v. 197, no. 3–4, p. 287-299.

-, 2004, Zirconolite: A new U-Pb chronometer for mafic igneous rocks: Geology, v. 32, no. 9, p. 785-788.

-, 2010, Dating sedimentary rocks using in situ U-Pb geochronology of syneruptive zircon in ash-fall tuffs <1 mm thick: Geology, v. 38, no. 4, p. 299-302.

Rasmussen, B., Fletcher, I. R., and McNaughton, N. J., 2001, Dating low-grade metamorphic events by SHRIMP U-Pb analysis of monazite in shales: Geology, v. 29, no. 10, p. 963-966.

Rasmussen, B., Mueller, A., and Fletcher, I., 2009, Zirconolite and xenotime U–Pb age constraints on the emplacement of the Golden Mile Dolerite sill and gold mineralization at the Mt Charlotte mine, Eastern Goldfields Province, Yilgarn Craton, Western Australia: Contributions to Mineralogy and Petrology, v. 157, no. 5, p. 559-572.

Rasmussen, B., and Muhling, J., 2007, Monazite begets monazite: evidence for dissolution of detrital monazite and reprecipitation of syntectonic monazite during low-grade regional metamorphism: Contributions to Mineralogy and Petrology, v. 154, no. 6, p. 675-689.

Rasmussen, B., and Muhling, J. R., 2009, Reactions destroying detrital monazite in greenschist-facies sandstones from the Witwatersrand basin, South Africa: Chemical Geology, v. 264, no. 1–4, p. 311-327.

Schandl, E. S., and Gorton, M. P., 2004, A textural and geochemical guide to the identification of hydrothermal monazite: Criteria for selection of samples for dating epigenetic hydrothermal ore deposits: Economic Geology, v. 99, no. 5, p. 1027.

Scherstén, A., Årebäck, H., Cornell, D., Hoskin, P., Åberg, A., and Armstrong, R., 2000, Dating mafic–ultramafic intrusions by ion-microprobing contact-melt zircon: examples from SW Sweden: Contributions to Mineralogy and Petrology, v. 139, no. 1, p. 115-125.

Scoates, J. S., Scoates, R. F. J., Wall, C. J., Friedman, R. M., and Couëslan, C. G., 2017, Direct dating of ultramafic sills and mafic intrusions associated with Ni-sulfide mineralization in the Thompson Nickel Belt, Manitoba, Canada: Economic Geology, v. 112, no. 3, p. 675.

Seydoux-Guillaume, A.-M., Montel, J.-M., Bingen, B., Bosse, V., de Parseval, P., Paquette, J.-L., Janots, E., and Wirth, R., 2012, Low-temperature alteration of monazite: Fluid mediated coupled dissolution–precipitation, irradiation damage, and disturbance of the U–Pb and Th–Pb chronometers: Chemical Geology, v. 330–331, p. 140-158.

Stark, J. C., Wang, X.-C., Li, Z.-X., Denyszyn, S. W., Rasmussen, B., and Zi, J.-W., 2018, 1.39 Ga mafic dyke swarm in southwestern Yilgarn Craton marks Nuna to Rodinia transition in the West Australian Craton: Precambrian Research, v. 316, p. 291-304.

Tack, L., Wingate, M. T. D., De Waele, B., Meert, J., Belousova, E., Griffin, B., Tahon, A., and Fernandez-Alonso, M., 2010, The 1375Ma “Kibaran event” in Central Africa: Prominent emplacement of bimodal magmatism under extensional regime: Precambrian Research, v. 180, no. 1, p. 63-84.

Upton, B. G. J., Rämö, O. T., Heaman, L. M., Blichert-Toft, J., Kalsbeek, F., Barry, T. L., and Jepsen, H. F., 2005, The Mesoproterozoic Zig-Zag Dal basalts and associated intrusions of eastern North Greenland: mantle plume–lithosphere interaction: Contributions to Mineralogy and Petrology, v. 149, no. 1, p. 40-56.

Verbaas, J., Thorkelson, D. J., Milidragovic, D., Crowley, J. L., Foster, D., Daniel Gibson, H., and Marshall, D. D., 2018, Rifting of western Laurentia at 1.38 Ga: The Hart River sills of Yukon, Canada: Lithos, v. 316-317, p. 243-260.

Wilhelmij, H. R., and Cabri, L. J., 2016, Platinum mineralization in the Kapalagulu Intrusion, western Tanzania: Mineralium Deposita, v. 51, no. 3, p. 343-367.

Williams, I. S., 2001, Response of detrital zircon and monazite, and their U–Pb isotopic systems, to regional metamorphism and host-rock partial melting, Cooma Complex, southeastern Australia*: Australian Journal of Earth Sciences, v. 48, no. 4, p. 557-580.

Williams, M. L., Jercinovic, M. J., Harlov, D. E., Budzyń, B., and Hetherington, C. J., 2011, Resetting monazite ages during fluid-related alteration: Chemical Geology, v. 283, no. 3–4, p. 218-225.

Williams, M. L., Jercinovic, M. J., and Hetherington, C. J., 2007, Microprobe Monazite Geochronology: Understanding Geologic Processes by Integrating Composition and Chronology: Annual Review of Earth and Planetary Sciences, v. 35, no. 1, p. 137-175.

Wilson, M., 1992, Magmatism and continental rifting during the opening of the South Atlantic Ocean: a consequence of Lower Cretaceous super-plume activity?: Geological Society, London, Special Publications, v. 68, no. 1, p. 241-255.

Zi, J.-W., Gregory, C. J., Rasmussen, B., Sheppard, S., and Muhling, J. R., 2017, Using monazite geochronology to test the plume model for carbonatites: The example of Gifford Creek Carbonatite Complex, Australia: Chemical Geology, v. 463, p. 50-60.

Zi, J.-W., Rasmussen, B., Muhling, J. R., and Fletcher, I. R., 2018, U-Pb geochronology of monazite in Precambrian tuffs reveals depositional and metamorphic histories: Precambrian Research, v. 313, p. 109-118.

Zi, J.-W., Rasmussen, B., Muhling, J. R., Fletcher, I. R., Thorne, A. M., Johnson, S. P., Cutten, H. N., Dunkley, D. J., and Korhonen, F. J., 2015, In situ U–Pb geochronology of xenotime and monazite from the Abra polymetallic deposit in the Capricorn Orogen, Australia: Dating hydrothermal mineralization and fluid flow in a long-lived crustal structure: Precambrian Research, v. 260, no. 0, p. 91-112.

Figure Captions

Figure 1

Geological map showing distribution of the Karagwe-Ankole Belt (KAB) metasedimentary rocks, granitoids and mafic-ultramafic intrusions in the Kabanga-Musonggati alignment and adjoining areas. The inset map shows location and extent of the recently redefined KAB and the Kibaran Belt (KIB) (modified after Tack et al. 2010, Fernandez-Alonso et al. 2012, Evans et al. 2016 and references therein)

Figure 2

(A) Schematic geological map and cross section of the Kabanga area showing main lithologies and their distribution. (B) Local map showing outcrop and surface projections of mafic-ultramafic intrusions and massive sulfide ore bodies. Locations of selected drill-holes are also shown. (C) Cross section showing outlines of Kabanga Main and MNB (Main North Body) intrusions and main ore zones. Maps and cross sections after Maier et al. (2010).

Figure 3

Drill-cores of Kabanga sedimentary rocks showing (A) Bleached contact zone in hornfels (best illustrated by the drill-cores on the right) adjacent to ultramafic rock, Kabanga Main, KN05-01, 138 m; (B) Sulfidic andalusite–muscovite schist, MNB, KN01-05, 538 m; and (C) Banded pelite, MNB, KN01-01, 1,645 m (from Maier et al. 2010). Photomicrographs of (D) gabbronorite containing igneous zircon and monazite, monazite is surrounded by a prominent pleochroic halo in biotite, sample WM5 from Kabanga Main, KN95-78, 211.1 m, (E) muscovite schist, sample K96 from MNB, KN01-01B, 1356.15 m; (F) skeletal monazite hosted in muscovite schist, sample K100 from Kabanga Upper, KSM06, 125.4 m; (G, H) muscovite schist hosting minute metamorphic monazite crystals under plane- and cross-polarized light, respectively, sample K100 from Kabanga Upper, KSM06, 125.4 m, and (I) banded pelite, sample K101 Kabanga Upper, KSM04, 150.4 m.

Figure 4

(A-C) Back-scattered electron (BSE) images of igneous monazite and zircon. Dashed ellipses mark the area of each grain analysed by SHRIMP. (D) Concordia plot and weighted mean ages of igneous monazite. (E) Concordia plot and weighted mean ages of igneous zircon. 1σ analytical uncertainties are displayed.

Figure 5

(A-D) BSE images of metamorphic monazite in muscovite schists (K99 and K100) from Kabanga. Dashed ellipses mark the area of each grain analysed by SHRIMP, in D the small analytical areas are indicated by black arrows. (E) Concordia plot and weighted mean ages of metamorphic monazite. 1σ analytical uncertainties are displayed.

Figure 6

(A-C) BSE images of metamorphic monazite in muscovite schists (K89) from Nyanzali. Dashed ellipses mark the area of each grain analyzed by SHRIMP, and are indicated by black arrows. (D, E) Concordia plots and weighted mean ages of metamorphic monazite. 1σ analytical uncertainties are displayed.

Figure 7

Th-U plot displaying contrasting Th and U concentrations between igneous and metamorphic monazites, and between the metamorphic monazites of different age groups.

Figure 8

(A-B) BSE images of metamorphic monazite in banded pelite (K101) from Kabanga. Dashed ellipses mark the area of each grain analysed by SHRIMP. (C) Concordia plot and weighted mean ages of metamorphic monazite. 1σ analytical uncertainties are displayed.

Figure 9

(A) Probability density plots and histograms of all analyses from metamorphic monazites showing the bimodal distribution of the older cluster which is resolvable into two ages (1402 ± 9 Ma and 1375 ± 8 Ma), plus a distinct younger cluster at 991 ± 16 Ma. (B) Dates from the igneous zircon and monazite are overlapping which together yielded a pooled, weighted mean $^{207}Pb/^{206}Pb$ age of 1390 ± 8 Ma. Pooled ages are quoted at 95% confidence level. 20 Ma bin width.

Figure 10

Summary diagram of geochronology results obtained in this study in comparison with published data (compiled in Table S2). Data source: 1-9, this study; 10-11, Maier et al. (2007); 12-20 and 27-28, Tack et al. (2010); 21-24, Deblond et al. (2001); 25-26, Mäkitie et al. (2014).

TABLE 1. SUMMARY OF GEOCHRONOLOGY SAMPLES AND RESULTS

Sample ID	Lithology	Dated mineral	Crystal morphology	Crystal size (μm)	Th content (wt.%)	Age* (Ma)	Av. Age† (Ma)
Igneous							
WM5	Gabbronorite	Monazite	Euhedral	50-70	~3	1391 ± 9	1390 ± 7
WM5	Gabbronorite	Zircon	Acicular, euhedral	Small	<0.05	1387 ± 10	
Metamorphic M I							
K99,	Muscovite schist	Monazite	Hypidioblast	15-30	9-20	1401± 10	1402 ± 9
K100	Muscovite schist	Monazite	Hypidioblast		15-20	1403± 15	
Metamorphic M II							
K89	Muscovite schist	Monazite	Skeletal poikiloblast	>300	~0.6	1379 ± 27	1375 ± 8
K96	Muscovite schist	Monazite	Skeletal poikiloblast	>300	~0.6	1374 ± 13	
K100	Muscovite schist	Monazite	Skeletal poikiloblast	>300	0.5-1	1375 ± 15	
Metamorphic M III							
K101	Banded pelite	Monazite	Hypidioblast/ xenoblast	Up to 100	0.8-2	991 ± 16	991 ± 16

Note:

*Weighted mean $^{207}Pb/^{206}Pb$ age (95% confidence level) of individual samples.

†Combined mean age (95% confidence level) calculated for each group.

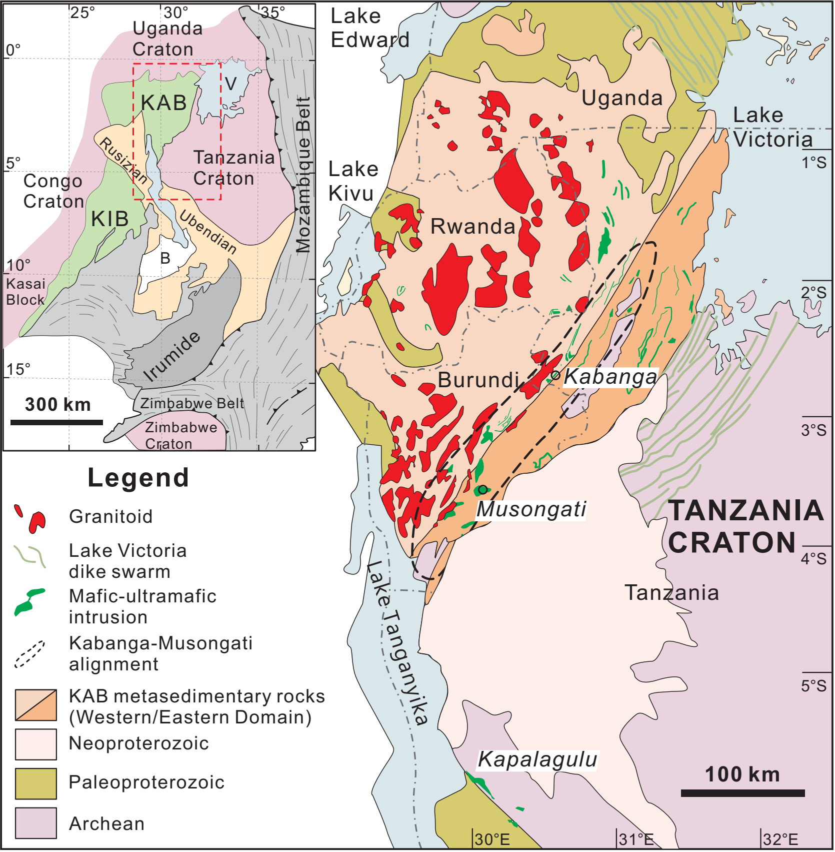

25°
30°
35°
0°
5°
10°
15°
Uganda Craton
KAB
V
Rusizian
Tanzania Craton
Congo Craton
KIB
Ubendian
Mozambique Belt
B
Kasai Block
Irumide
300 km
Zimbabwe Belt
Zimbabwe Craton
Legend
Granitoid
Lake Victoria dike swarm
Mafic-ultramafic intrusion
Kabanga-Musongati alignment
KAB metasedimentary rocks (Western/Eastern Domain)
Neoproterozoic
Paleoproterozoic
Archean
Lake Edward
Uganda
Lake Victoria
Lake Kivu
Rwanda
1°S
2°S
Burundi
Kabanga
3°S
Musongati
TANZANIA CRATON
4°S
Tanzania
Lake Tanganyika
5°S
Kapalagulu
100 km
30°E
31°E
32°E

Figure 1

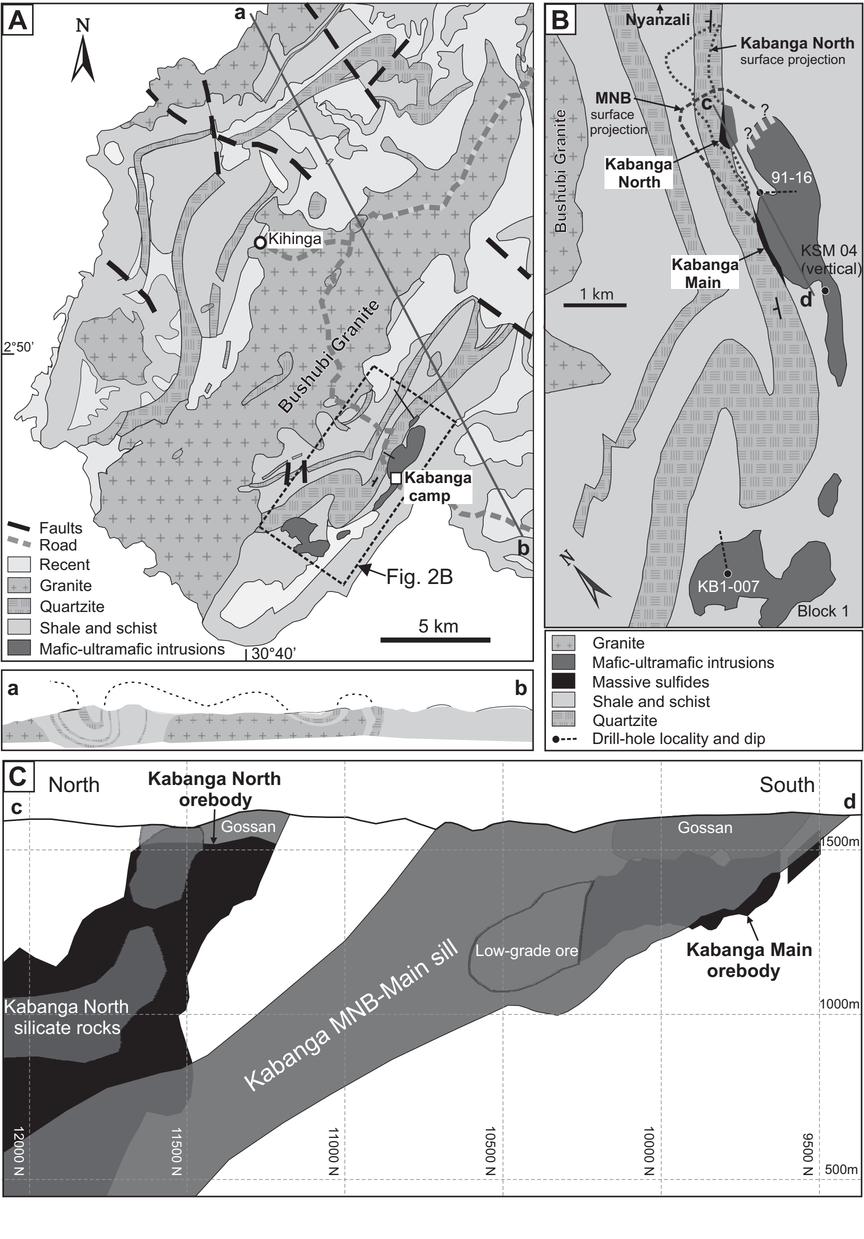
A
a
N
Kihinga
2°50'
Bushubi Granite
Kabanga camp
Fig. 2B
b
Faults
Road
Recent
Granite
Quartzite
Shale and schist
Mafic-ultramafic intrusions
5 km
30°40'
B
Nyanzali
Kabanga North surface projection
MNB surface projection
c
?
Bushubi Granite
Kabanga North
91-16
Kabanga Main
KSM 04 (vertical)
1 km
d
N
KB1-007
Block 1
Granite
Mafic-ultramafic intrusions
Massive sulfides
Shale and schist
Quartzite
Drill-hole locality and dip
a
b
C
North
Kabanga North orebody
South
c
d
Gossan
Gossan
1500m
Low-grade ore
Kabanga Main orebody
Kabanga MNB-Main sill
Kabanga North silicate rocks
1000m
12000 N
11500 N
11000 N
10500 N
10000 N
9500 N
500m

Figure 2

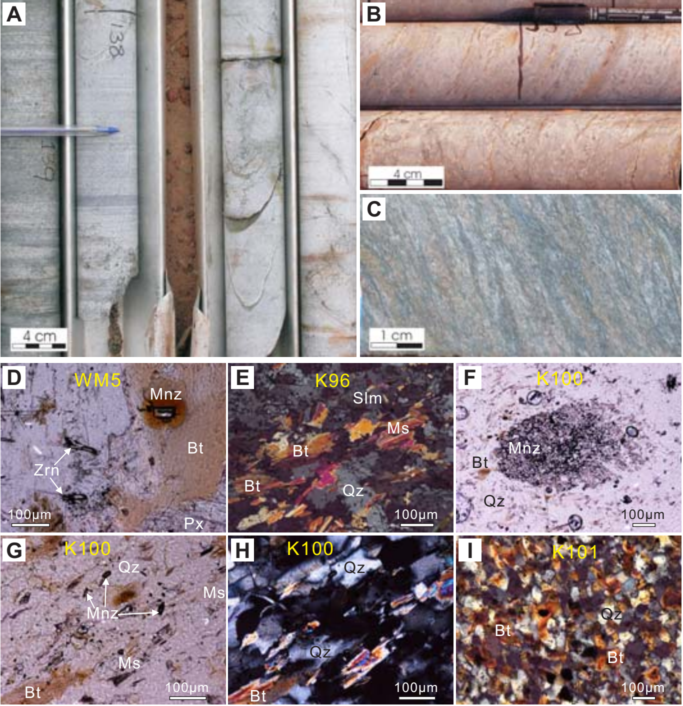
A
4 cm
B
4 cm
C
1 cm
D
WM5
Mnz
Bt
Zrn
Px
100μm
E
K96
Slm
Ms
Bt
Bt
Qz
100μm
F
K100
Mnz
Bt
Qz
100μm
G
K100
Qz
Ms
Mnz
Ms
Bt
100μm
H
K100
Qz
Qz
Bt
100μm
I
K101
Qz
Bt
Bt
100μm

Figure 3

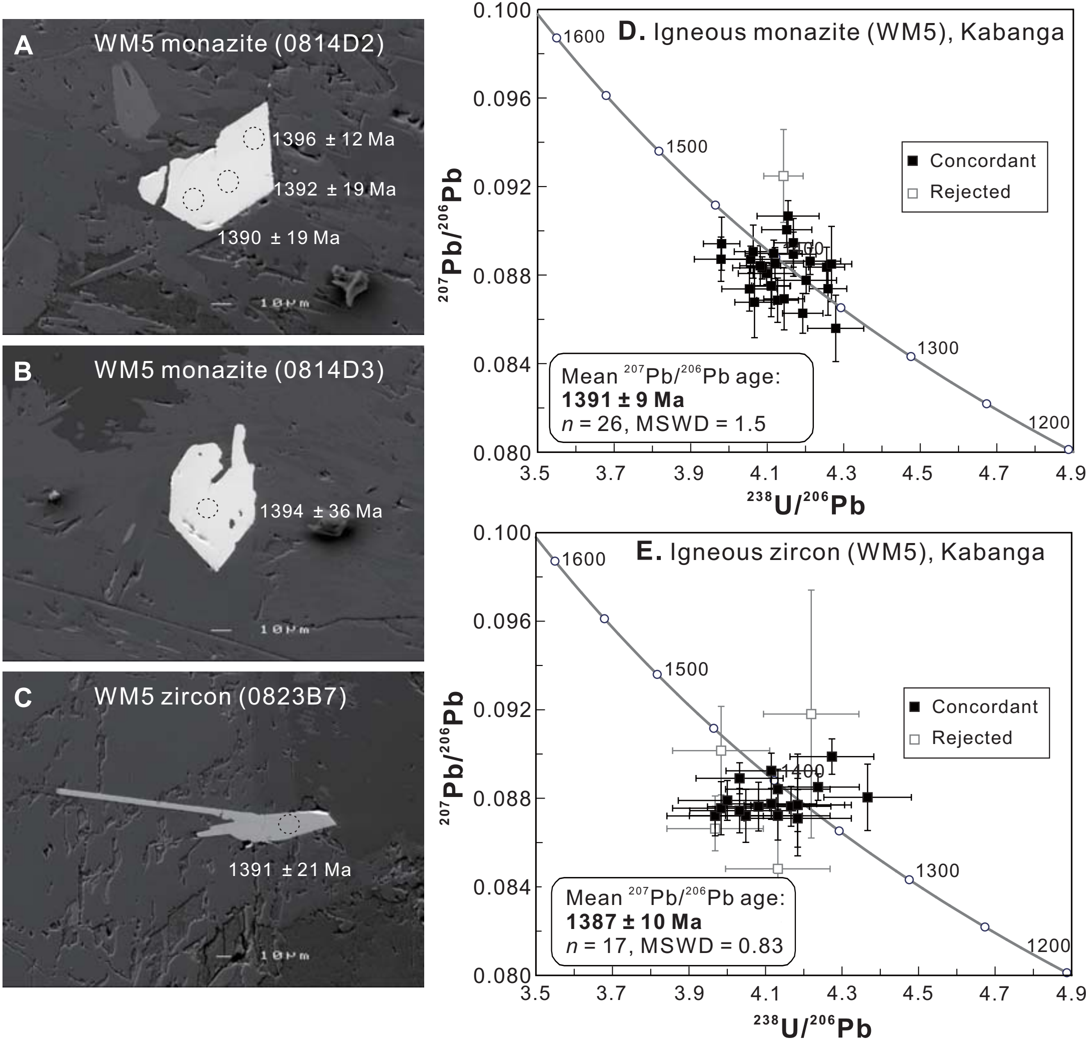
A
WM5 monazite (0814D2)
1396 ± 12 Ma
1392 ± 19 Ma
1390 ± 19 Ma
B
WM5 monazite (0814D3)
1394 ± 36 Ma
C
WM5 zircon (0823B7)
1391 ± 21 Ma
D. Igneous monazite (WM5), Kabanga
Concordant
Rejected
Mean 207Pb/206Pb age:
1391 ± 9 Ma
n = 26, MSWD = 1.5
E. Igneous zircon (WM5), Kabanga
Concordant
Rejected
Mean 207Pb/206Pb age:
1387 ± 10 Ma
n = 17, MSWD = 0.83
207Pb/206Pb
238U/206Pb
1600
1500
1400
1300
1200

Figure 4

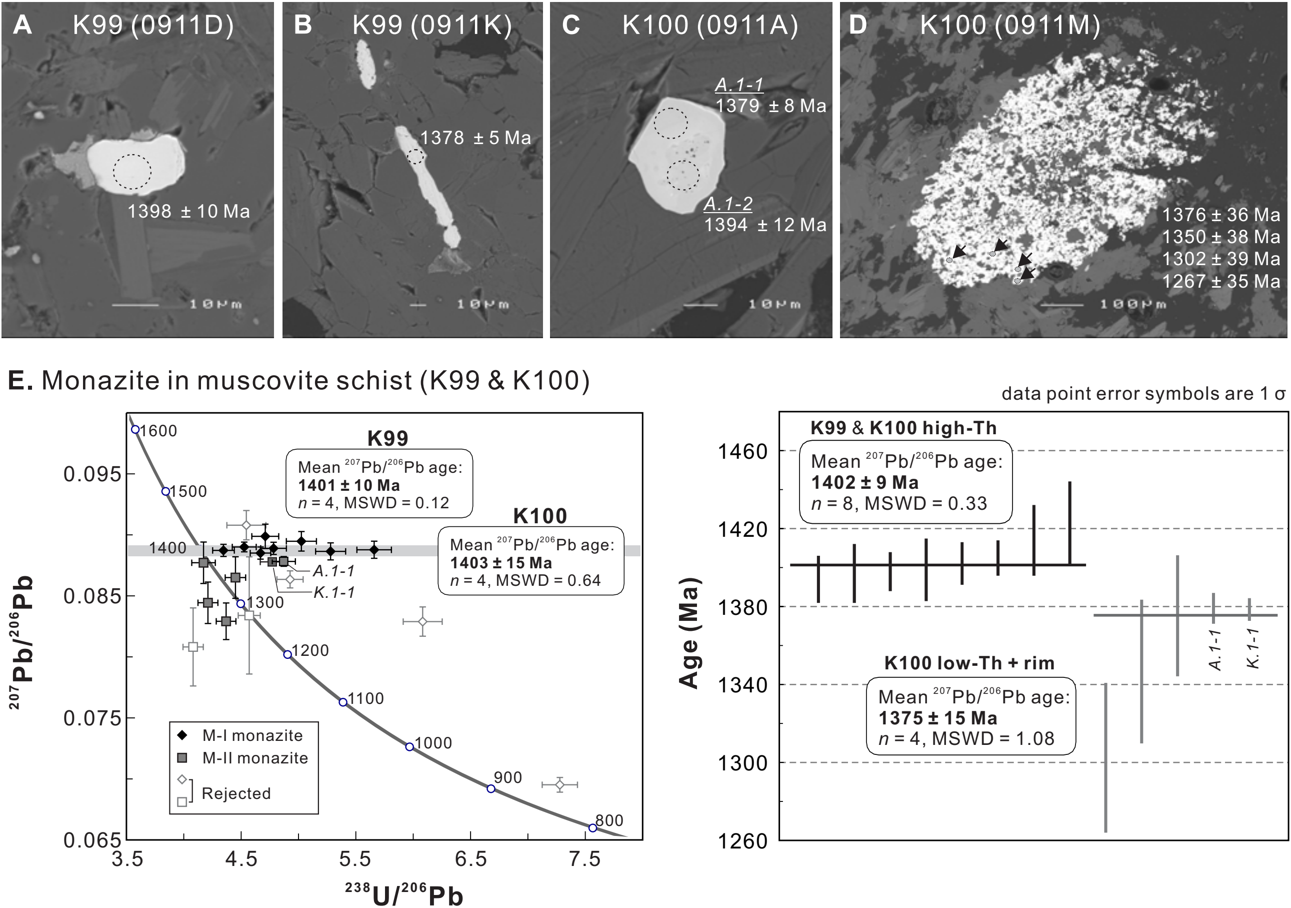

A K99 (0911D)
1398 ± 10 Ma
10μm
B K99 (0911K)
1378 ± 5 Ma
10μm
C K100 (0911A)
A.1-1
1379 ± 8 Ma
A.1-2
1394 ± 12 Ma
10μm
D K100 (0911M)
1376 ± 36 Ma
1350 ± 38 Ma
1302 ± 39 Ma
1267 ± 35 Ma
100μm
E. Monazite in muscovite schist (K99 & K100)
data point error symbols are 1 σ
K99
Mean 207Pb/206Pb age:
1401 ± 10 Ma
n = 4, MSWD = 0.12
K100
Mean 207Pb/206Pb age:
1403 ± 15 Ma
n = 4, MSWD = 0.64
A.1-1
K.1-1
M-I monazite
M-II monazite
Rejected
207Pb/206Pb
238U/206Pb
K99 & K100 high-Th
Mean 207Pb/206Pb age:
1402 ± 9 Ma
n = 8, MSWD = 0.33
K100 low-Th + rim
Mean 207Pb/206Pb age:
1375 ± 15 Ma
n = 4, MSWD = 1.08
Age (Ma)

Figure 5

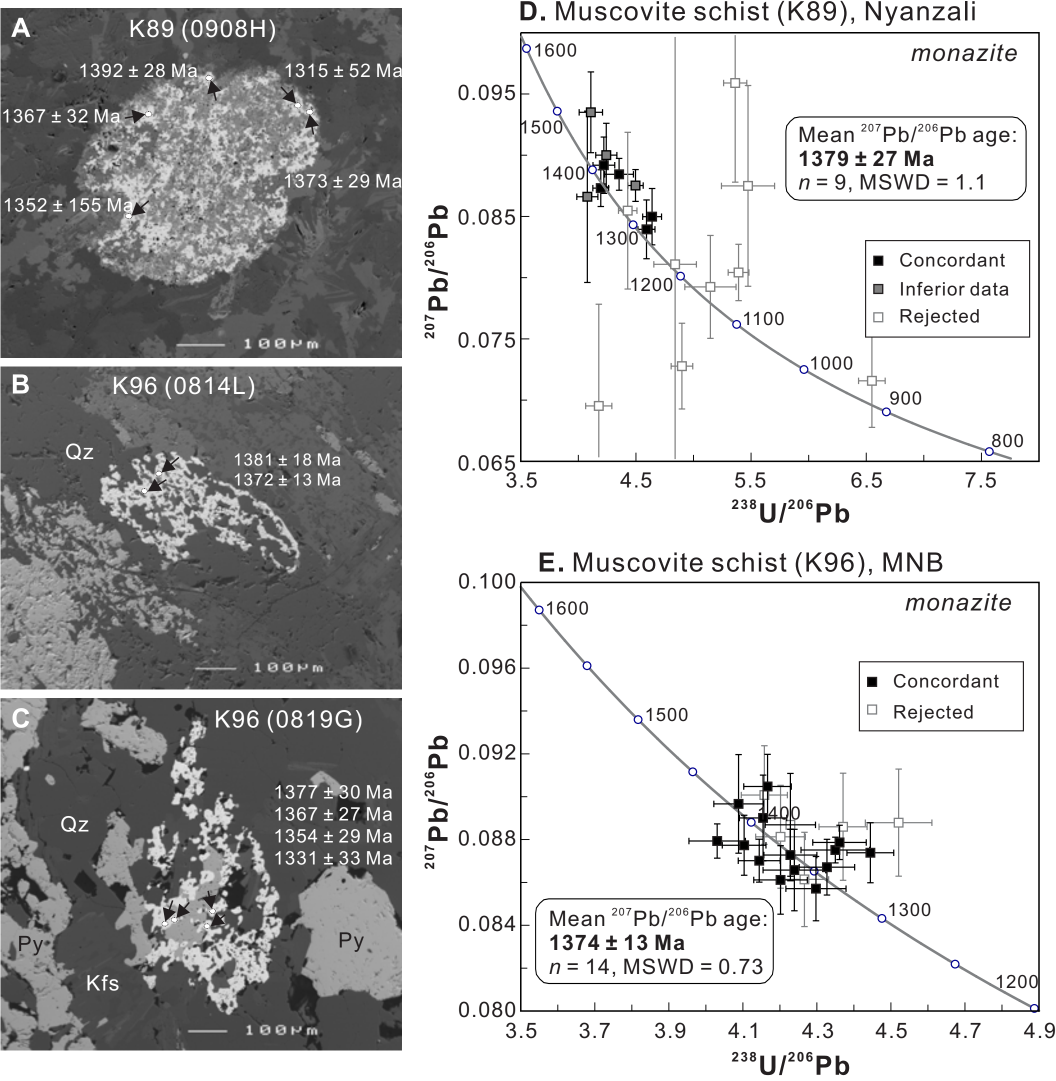
A
K89 (0908H)
1392 ± 28 Ma
1315 ± 52 Ma
1367 ± 32 Ma
1373 ± 29 Ma
1352 ± 155 Ma
100µm
B
K96 (0814L)
Qz
1381 ± 18 Ma
1372 ± 13 Ma
100µm
C
K96 (0819G)
Qz
1377 ± 30 Ma
1367 ± 27 Ma
1354 ± 29 Ma
1331 ± 33 Ma
Py
Py
Kfs
100µm
D. Muscovite schist (K89), Nyanzali
monazite
Mean 207Pb/206Pb age:
1379 ± 27 Ma
n = 9, MSWD = 1.1
Concordant
Inferior data
Rejected
1600
1500
1400
1300
1200
1100
1000
900
800
0.095
0.085
0.075
0.065
3.5
4.5
5.5
6.5
7.5
207Pb/206Pb
238U/206Pb
E. Muscovite schist (K96), MNB
monazite
Concordant
Rejected
Mean 207Pb/206Pb age:
1374 ± 13 Ma
n = 14, MSWD = 0.73
1600
1500
1400
1300
1200
0.100
0.096
0.092
0.088
0.084
0.080
3.5
3.7
3.9
4.1
4.3
4.5
4.7
4.9
207Pb/206Pb
238U/206Pb

Figure 6

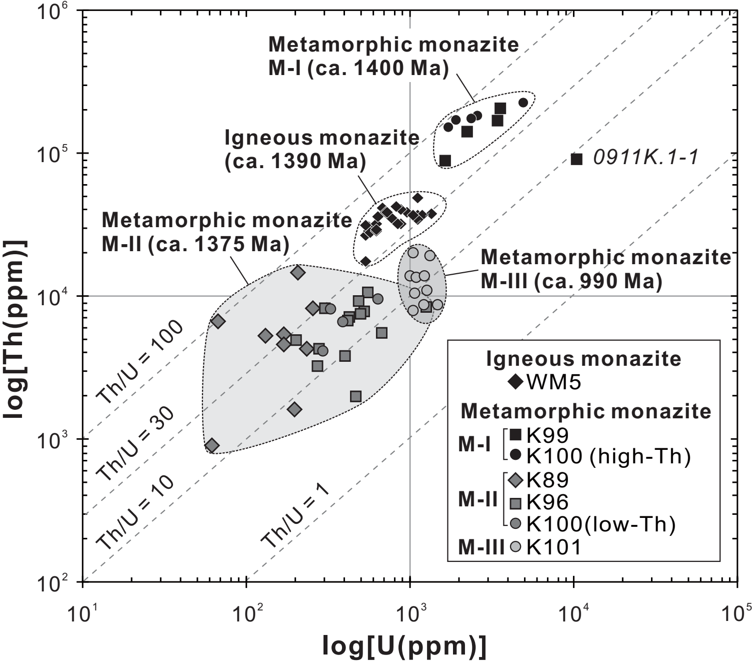

Metamorphic monazite
M-I (ca. 1400 Ma)
Igneous monazite
(ca. 1390 Ma)
Metamorphic monazite
M-II (ca. 1375 Ma)
Metamorphic monazite
M-III (ca. 990 Ma)
0911K.1-1
Th/U = 100
Th/U = 30
Th/U = 10
Th/U = 1
Igneous monazite
WM5
Metamorphic monazite
M-I
K99
K100 (high-Th)
M-II
K89
K96
K100(low-Th)
M-III
K101
log[Th(ppm)]
log[U(ppm)]
10^6
10^5
10^4
10^3
10^2
10^1
10^2
10^3
10^4
10^5

Figure 7

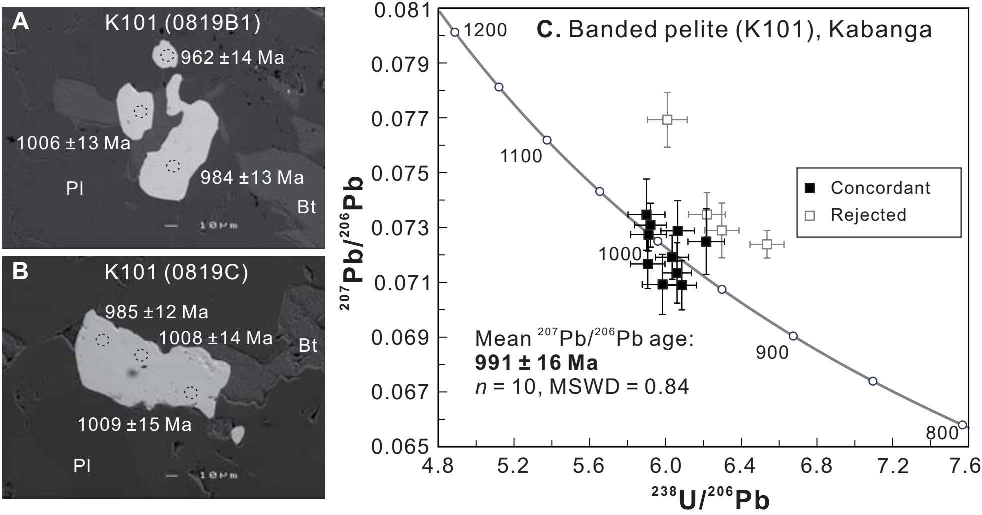
A
K101 (0819B1)
962 ±14 Ma
1006 ±13 Ma
984 ±13 Ma
Pl
Bt
B
K101 (0819C)
985 ±12 Ma
1008 ±14 Ma
Bt
1009 ±15 Ma
Pl
C. Banded pelite (K101), Kabanga
Concordant
Rejected
Mean 207Pb/206Pb age:
991 ± 16 Ma
n = 10, MSWD = 0.84
1200
1100
1000
900
800
207Pb/206Pb
238U/206Pb

Figure 8

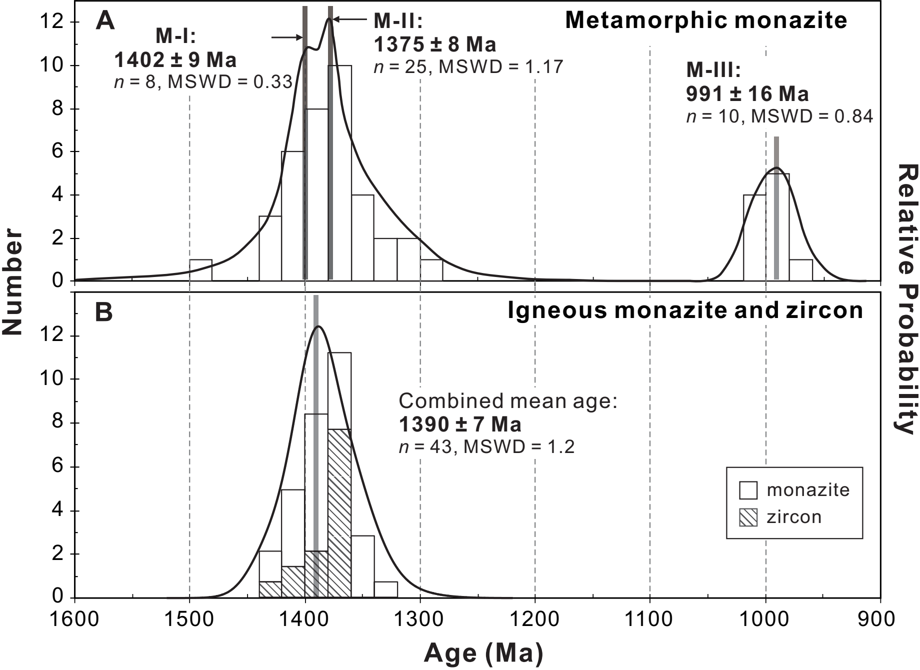

A
Metamorphic monazite
M-I:
1402 ± 9 Ma
n = 8, MSWD = 0.33
M-II:
1375 ± 8 Ma
n = 25, MSWD = 1.17
M-III:
991 ± 16 Ma
n = 10, MSWD = 0.84
B
Igneous monazite and zircon
Combined mean age:
1390 ± 7 Ma
n = 43, MSWD = 1.2
monazite
zircon
Number
Relative Probability
Age (Ma)
1600
1500
1400
1300
1200
1100
1000
900
0
2
4
6
8
10
12

Figure 9

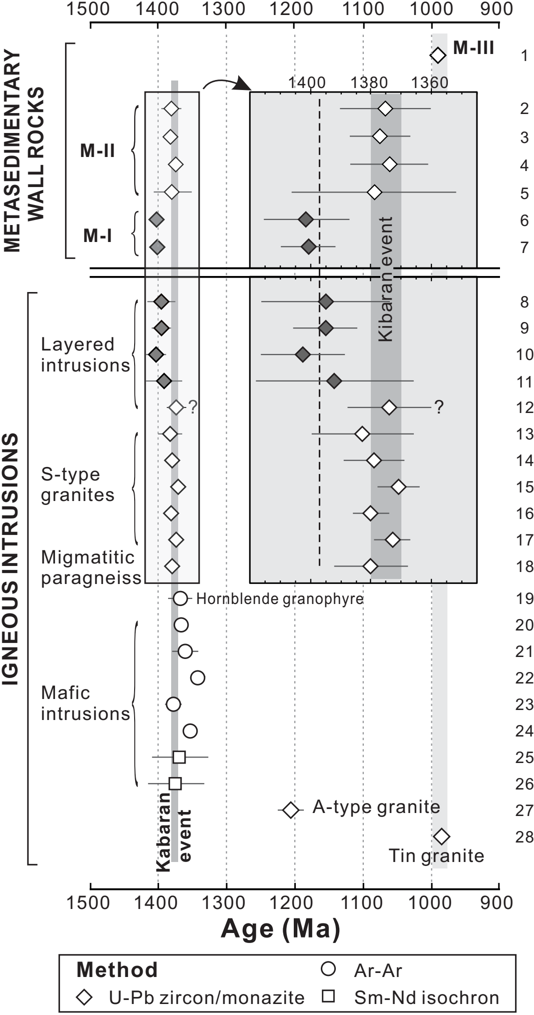

1500 1400 1300 1200 1100 1000 900
1400 1380 1360
METASEDIMENTARY WALL ROCKS
M-III
M-II
M-I
Kibaran event
IGNEOUS INTRUSIONS
Layered intrusions
S-type granites
Migmatitic paragneiss
Hornblende granophyre
Mafic intrusions
A-type granite
Tin granite
Kabaran event
1 2 3 4 5 6 7 8 9 10 11 12 13 14 15 16 17 18 19 20 21 22 23 24 25 26 27 28
Age (Ma)
Method
Ar-Ar
U-Pb zircon/monazite
Sm-Nd isochron

Figure 10